Proceedings of the ASME-JSME-KSME 2011 Joint Fluids Engineering Conference
AJK-Fluids2011
July 24-29, 2011, Hamamatsu, Shizuoka, JAPAN

AJK2011-08001

# INVESTIGATION OF ROD VIBRATIONS IN DROPLET TWO-PHASE FLOWS

**Yoshiteru Komuro**
Department of nuclear engineering, Kyoto Univ.
Yoshida-honmachi, Sakyo-ku,
Kyoto-shi, Kyoto, Japan

**Zensaku Kawara**
Department of nuclear engineering, Kyoto Univ.
Yoshida-honmachi, Sakyo-ku,
Kyoto-shi, Kyoto, Japan

**Tomoaki Kunugi**
Department of nuclear engineering, Kyoto Univ.
Yoshida-honmachi, Sakyo-ku,
Kyoto-shi, Kyoto, Japan

## ABSTRACT

Flow-induced vibrations are important problems in nuclear power plants from the view point of reactor safety. In the investigations of these vibrations especially those induced by two-phase flows, a numerical simulation plays a significant role, so it is necessary to obtain the experimental datasets that can validate the results of the numerical simulation. This paper deals with the experimental data of one-end-supported rod vibration, and focuses on the differences between the rod vibrations induced by single-phase air flows and those induced by droplet two-phase flows. In the experiments, the displacement of the non-supported end of the test rod was visualized by the high speed camera with high spatial and temporal resolutions, namely 9.5 μm and 500 μsec. Using an image analyzing software, the rod vibration displacements were measured by the motion tracking method. The curved surface of the rod was observed by another high speed camera and the relationship between the rod vibrations and the wet condition on the surface of the rod was investigated. In addition, the vibrations measured by the strain gages and those by the high speed camera were compared to discuss the differences in these two ways of the measurements.

## 1. INTRODUCTION

Flow-induced vibrations (FIV) are very important problems in nuclear power plants from the safety point of view. If a cross-flow consists of two phases, the characteristics of FIV become more complicated than those in a single-phase flow. In the present work, vibrations induced by cross-flows are investigated because cross-flows or velocity components in the cross-flow directions are very significant causes of structure vibrations in reactor cores as well as steam generators [1]. As for the FIV in the water-vapor two-phase cross-flows, a lot of studies have been carried out. For example, one-end-supported rod vibrations have been studied in detail, considering a void fraction as an important parameter of the two-phase cross-flow [2]. In addition, the effects of the vapor voids on the rod vibration reduction were reported by Hara [3] and Ogawa [4]. In each of these experimental studies, a single rod was used. On the other hand, the studies on the vibrations of a tube array or tubes used in heat exchangers induced by two-phase cross-flows have also been reported [5-7]. To the contrary, there is no experimental study regarding a rod vibration induced by the gas cross-flow including water droplets, except for some large scale experiments on "rain vibrations".

Rod vibrations induced by air cross-flow including water droplets have been studied on rain vibrations. This phenomenon was observed at some real bridges and large scale experimental bridges [8], and is considered to have a strong relationship with water droplets on the surface of cables of the bridges. In the experimental studies, a two-side-supported cylinder was often used as an analytical model of cables. Yamaguchi made an analytical study on the relationship of the water rivulet on the surface of cables and the cable vibrations [9]. The experimental studies on rain vibrations were conducted only in the real scale [10] or the large scale systems [11] because the small scale experimental systems cannot realize either of the real condition or its similarity conditions of the rain vibrations.

It is difficult to analyze the interactions between the droplets and the rod, and to evaluate the effect of the surface wet conditions on the rod vibrations. Therefore, in the investigations of these vibrations especially those induced by two-phase flow, numerical simulation plays a significant role, then it is necessary to obtain enough experimental data sets that can validate the results of the simulation. This paper deals with the experimental data of one-end-supported rod vibration, referring to the differences in vibration amplitudes attributed to whether or not the air flow includes the water droplets. In addition, the vibrations measured by the strain gages and those by the high speed camera were compared to discuss the differences in these two ways of the measurements.

## 2. NOMENCLATURE

| | | |
|---|---|---|
| D | diameter | [m] |
| $f_0$ | natural frequency | [Hz] |
| g | acceleration of the gravity | [m·s$^{-2}$] |
| L | length | [m] |
| ε | magnitude of strain | [-] |
| σ | displacement (R.M.S.) | [-] |

**Subscripts**

| | |
|---|---|
| c | cylinder (test rod) |
| g | gas (air), strain gage |
| w | water droplet |
| x | Lift direction |
| y | Drag direction |

## 3. EXPERIMENT

### 3.1 Experimental Apparatus

Figure 1 shows the schematic of experimental apparatus. The dry air from an air compressor comes into the test section from the two inlets on the opposite walls and flows uniformly downward in the test section. The test section is a transparent acrylic rectangular duct with 160 mm×40 mm horizontal cross section. The one-end-supported rod (hereafter, called "test rod") is fixed rigidly at the wall of test section as shown in Fig. 2. The axis of the test rod is set at 660 mm downstream from the inlet of the air flow. A water injection needle is set at 360 mm upstream from the axis of the test rod in order to put the pure water droplets into the air flow.

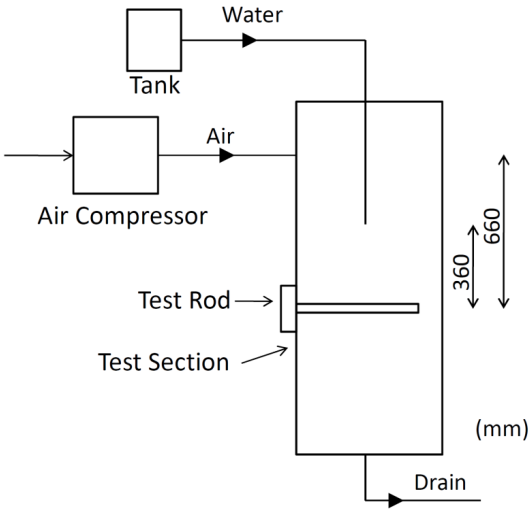


**FIGURE 1.** SCHEMATIC OF EXPERIMENTAL APPARATUS

### 3.2 Test Rods

In the present study, four different cylindrical test rods were used. The physical properties and the structural parameters of each test rod are shown in Table 1. The natural frequencies of test rods were experimentally measured before any other experiments with air flow. The natural frequency $f_0$ and the structural damping ratio ζ were determined from the attenuation curves of the arbitral rod vibration. A logarithmic decrement $\delta$ is defined as $\delta = 2\pi\zeta/\sqrt{1-\zeta^2}$ [12].

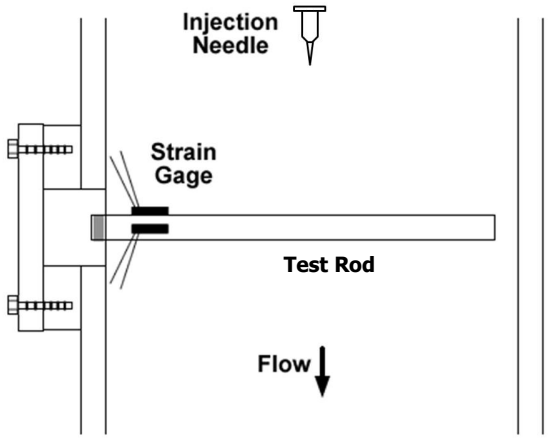


**FIGURE 2.** LAYOUT OF TEST SECTION

### 3.3 High Speed Camera System

Recently, high speed video imaging systems have been upgraded significantly on the number of pixels, recording speed and optical sensitivity, and this enables the application of the combination of the high speed video system and the long-ranged microscope in order to observe very small vibrations whose amplitudes are micron meter order of the spatial resolution and sub-millisecond order of the temporal one. In the present study, the movements of a target mark, which had been carved at the center of the test rod's free-end face, were visualized by using the Cassegrain optical system (Seika Co., Japan), and the high speed video camera (Phantom 7.1, Vision Research Co., USA). The working distance of the Cassegrain optical system was 640 mm, and the finest spatial resolution of this system was 9.5 μm per pixel of the image data. The frame rate of recording was 2000 frames per second and 1450 frames were obtained at each measurement.

In addition, the wet condition on the curved surface of the test rod was observed by using another high speed camera (FASTCAM 512PCI, Photron Co., Japan). The setup positions of two high speed cameras are shown in Fig. 3. The schematic of the experimental apparatus shown in Fig. 3 describes a horizontal cross section of the acrylic test section and the test rod. The field of view was 5.0 cm×5.0 cm and the spatial resolution was 98 μm per pixel. The frame rate of recording was set to 1000 frames per second. It was arranged that the FASTCAM could send a start trigger to the Phantom, which enables a simultaneous recording by means of two high speed cameras.

**TABLE 1.** PARAMETERS OF TEST RODS

| Rod No. | Diameter $D_c$ [mm] | Length $L_c$ [mm] | Aspect Ratio (=$L_c/D_c$) | Natural Frequency $f_0$ [Hz] | Logarithmic Decrement δ |
|---|---|---|---|---|---|
| #1 | 10.0 | 150.0 | 15 | 108 | 0.14 |
| #2 | 6.0 | 150.0 | 25 | 72.7 | 0.15 |
| #3 | 6.0 | 90.0 | 15 | 197 | 0.15 |
| #4 | 4.0 | 100.0 | 25 | 100 | 0.20 |

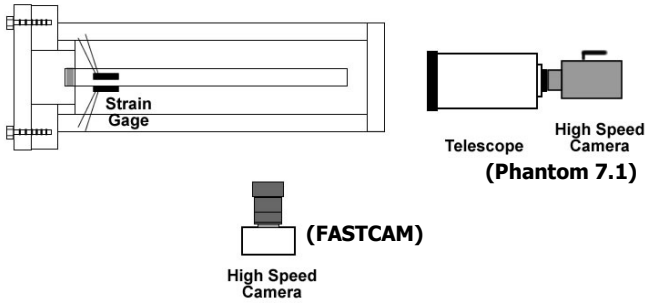


**FIGURE 3.** LAYOUT OF HIGH SPEED CAMERAS

### 3.4 Experimental Procedures

**Single-phase Flow Experiment:** As the reference experiments, the test rod vibrations induced by the single-phase air flow were investigated. In these experiments the dry air was used as the working fluid. The flow rate was adjusted by a valve, ranging from 0 to 4000 L/min. The test rods #1 to #4 were used in order to measure the vibration of each rod by the strain gages and, with regard to the test rods #1 and #2, the vibrations were also observed by the high speed camera system simultaneously with the strain gages measurements. At the rigid end of each test rod, two strain gages were glued to the curved surface (see Figs. 2 and 3) in order to measure the strain magnitudes of the test rod in the "Drag" direction, which is parallel to the flow direction, and in the "Lift" direction, which is perpendicular to both of the flow direction and the axial direction. The sampling rate of the strain gages were 10 kHz and the duration of each measurement was 2 sec.

**Droplet Two-phase Flow Experiments:** The droplet two-phase flow that consisted of the air flow and the pure water droplets injected from the injection needle as shown in Fig. 2 with the flow rate: 2-4 mL/s, was used as the working fluid. The flow rate of air was adjusted by the valve, ranging from 0 to 4000 L/min. The inner and outer diameters of the injection needle (25G) are 0.312 mm and 0.516 mm, respectively. Setting the test rods #1 and #2 at the test port sequentially, the vibration of each rod was observed by the high speed camera system (Phantom) and the wet condition on the curved surface of each rod was simultaneously observed using another high speed video camera (FASTCAM). Measurements at the flow rate of 2000, 2500, 3000, 3500 and 4000 L/min were conducted three times and, at the second and third measurements, the rod vibration was measured by the strain gages instead of using the high speed cameras. In addition, the vibrations of test rods #1 and #2 at the flow rate of 3200, 2800, 2300 (only for the test rod #1), 2200 (only for the test rod #2) and 1800 L/min were measured by the strain gages. The sampling rate of the strain gages were 10 kHz and the duration of each measurement was 2 sec.

## 4. RESULTS AND DISCUSSIONS

### 4.1 Single-phase Flow Experiments

In order to organize the experimental data for the various test rods as shown in Table 1, a reduced velocity Vr is employed. The Vr is a dimensionless parameter and is defined by Eq. (1). $U_g$ denotes a superficial velocity of air flow, which is defined as the flow rate divided by the cross-section area of the flow channel.

$$\mathrm{Vr} = \frac{\mathrm{U_g}}{f_0 \mathrm{D_c}} \tag{1}$$

The magnitude of the strain of test rod at the position of the strain gage is calculated from the output voltages of the strain gages. If the air flow is uniform in the Lift direction, the strain value ε can be converted by Eq. (2) into a displacement of the head of each test rod in the Lift direction or in the Drag direction, represented by x in Eq. (2) (a similar way of converting the strain into the displacement is seen in [13]). $L_c$ and $L_g$ represent the axial length of the test rod, and the distance from the rigid edge of the test rods to the center of the strain gage, respectively.

$$\mathrm{x} = \frac{{\mathrm{L_c}}^4}{2\mathrm{D_c}\left(\mathrm{L_c} - \mathrm{L_g}\right)^2}\varepsilon \tag{2}$$

The root-mean-square (R.M.S.) values of the vibration displacements in the Lift and Drag directions ( $\sigma_{x,rms}$ and $\sigma_{y,rms}$) are calculated from the displacement of the test-rod end converted from the strain values, and then the R.M.S. power ratio $\sigma_{ratio}$ defined as Eq. (3) is able to be obtained. This ratio indicates the degree to which the kinetic energy of vibration is biased toward the Lift direction.

$$\sigma_{\mathrm{ratio}} = \frac{{\sigma_{\mathrm{x,rms}}}^2}{{\sigma_{\mathrm{x,rms}}}^2 + {\sigma_{\mathrm{y,rms}}}^2} \tag{3}$$

The dimensionless vibration displacements, which are the R.M.S. values of vibration displacements divided by the diameter of each test rod, in the Lift and Drag directions are shown in Fig. 4. Regarding the dimensionless displacements in the Lift direction, there are two peaks at the Vr below 10. This means when the frequency of a vortex shedding from the test rod is close to the natural frequency of the test rod, a resonance occurs, and then the displacement of the vibration becomes larger. In contrast, no peak was seen in the Drag direction. The cause is presumably the confinement effect of the test section on the vortex shedding, since the width of the test section in the Lift direction is 40 mm whereas the diameter of test rods are 4-10 mm. When the vortexes are not fully developed, the magnitude of the forces in the Drag direction that the test rods experience from the downstream vortexes shows a decline compared to those for a fully developed situation. As for the Lift direction, when the vortexes are shedding from one side after the other side alternately, it is considered that the test rods experience the forces of the vortex shedding from the downstream even though the vortexes are not fully developed. Meanwhile, in the Drag direction, the dimensionless amplitudes $A_y/D_c$ of the test rods #1, #2 and #3 are essentially proportional to the square of the reduced velocity. These characteristics correspond with those of the random excitations [14].

In order to investigate the frequency components in the variation of the displacement of test rod end against time, the fast Fourier transformation (FFT) method is used. The results of the FFT for time variation of the edge displacement in the Lift direction of the test rod #1 are shown in Fig. 5. There are three spectra for the different reduced velocities of 5.6, 6.8 and 8.4, and every spectrum has a peak at the natural frequency of the test rod #1. In the cases of the Vr of 6.8 and 8.4, the spectra have another peak that is wide ranged in the frequency. The frequency values the peak contains become lower as the reduced velocity becomes small. In case of the reduced velocity of 5.6, two peaks coalesce into a single peak and the dimensionless vibration in the Lift direction also has a peak at this Vr (see Fig. 4 (a)).

Vortex shedding frequency $f_w$ from the cylindrical test rod is expressed as Eq. (4) where St is the Strouhal number of the test rod [15].

$$f_w = \mathrm{St}\frac{U_g}{D_c} \tag{4}$$

The decrease in the reduced velocity means the decrease in the $U_g$. Thus, the broad peak in vibration frequency, which is considered to be caused by vortex shedding, moves toward lower values as the reduced velocity decreases. In case of the Vr of 5.6, $f_w$ becomes equal to $f_0$, which means that the Strouhal number of the rod #1 is 0.18.

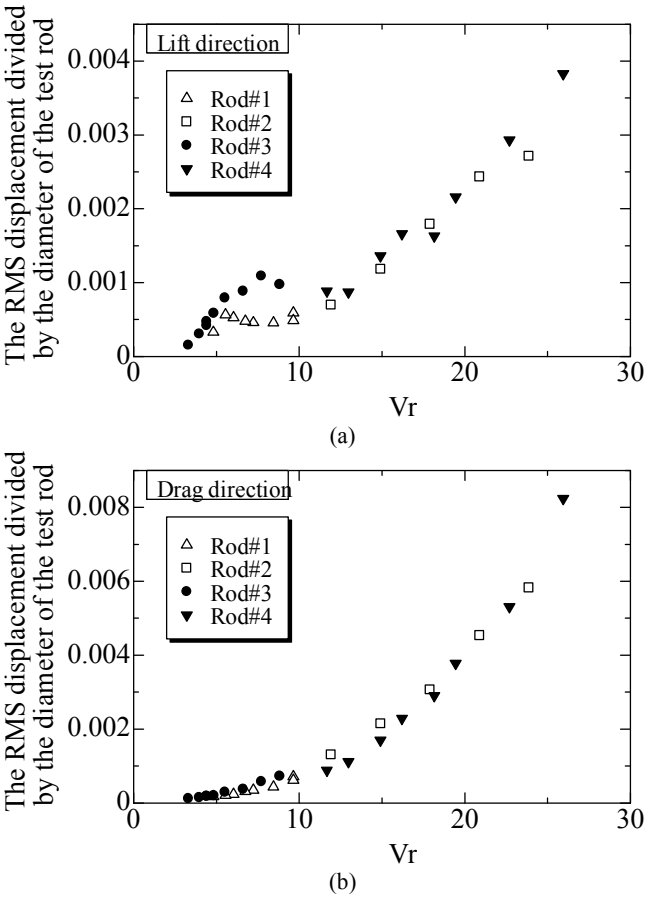


**FIGURE 4.** R.M.S. VALUES OF DIMENSIONLESS VIBRATION DISPLACEMENTS
(a) Lift direction (b) Drag direction

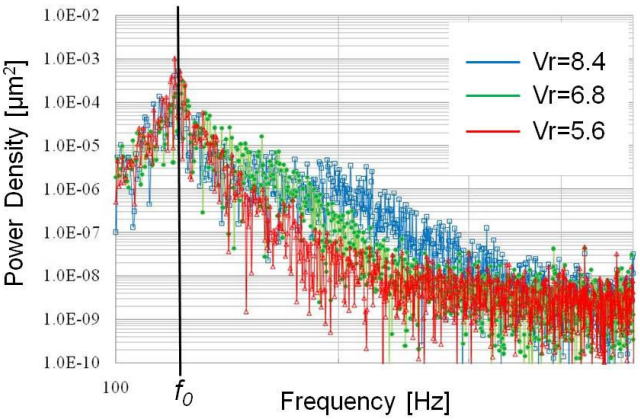


**FIGURE 5.** POWER DENSITY OF FREQUENCY COMPONENTS IN ROD VIBRATIONS (Rod #1, Lift direction)

### 4.2 Droplet Two-Phase Flow Experiments

Figure 6 shows the droplets behavior after colliding on the curved surface of the test rods #1 and #2 at two different $U_g$ of 10.4 and 6.0 m/s. There is a clear tendency that the smaller the

air flow rate is, the more and larger droplets stay on the surface of the test rod. This is because in the larger air flow the droplets on the surface move faster, slide downward along the curved surface, and detach more easily. The diameters of the droplets in Figure 6 (a) are about 1-2 mm before colliding with the test rod, and around 2 mm on the upper surface of the rod. In the recorded images, no splash was observed when a droplet collided with the test rod.

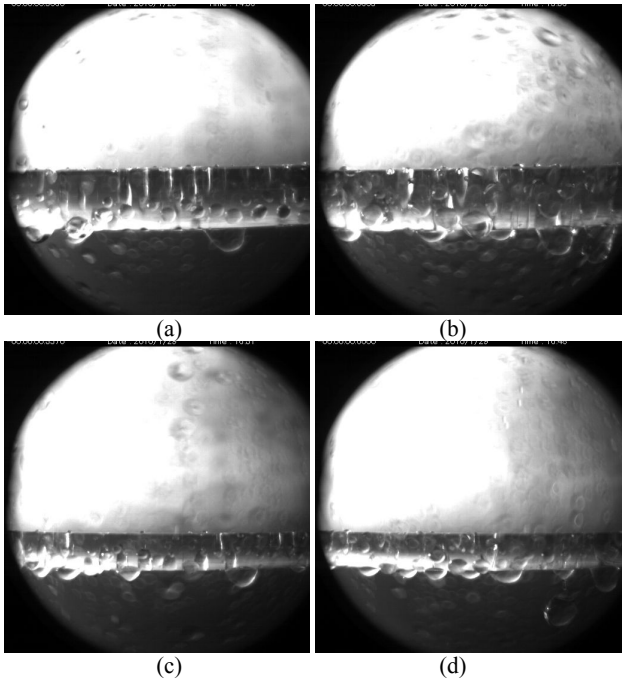


**FIGURE 6.** DROPLETS BEHAVIOR AFTER COLLIDING ON THE CURVED SURFACE OF THE TEST RODS
(a) Rod #1, $U_g$=10.4 m/s (b) Rod #1, $U_g$=6.0 m/s
(c) Rod #2, $U_g$=10.4 m/s (d) Rod #2, $U_g$=6.0 m/s

Droplet velocities just before colliding to the rod surface are obtained from the image analyses. These data are plotted on Fig. 7 with circle symbols. In addition, the droplet velocities at the vertical position of the upper surface of the test rods are numerically calculated by assuming droplets as hard spheres. The one-dimensional equation of motion is described as Eq. (5), where $u_w$ and $u_g$ denote the velocities of the water droplet and air flow respectively, $\rho_w$ and $\rho_g$ denote the densities of water and air respectively, and m is the mass of the water droplet. $C_D$ is the drag coefficient of spherical particles and is expressed as Eq. (6) proposed by Haider and Levenspiel [16].

$$\frac{du_w}{dt} = -\frac{1}{2m} C_D \rho_g \frac{\pi D_w^2}{4} (u_w - u_g)|u_w - u_g| + g\left(1 - \frac{\rho_g}{\rho_w}\right) \quad (5)$$

$$C_D = \frac{24}{Re}(1 + 0.1806Re^{0.6459}) + \frac{0.4251}{1 + \frac{6880.95}{Re}} \quad (6)$$

The particle Reynolds number Re is described as Eq. (7) where $\nu_g$ denotes the kinetic viscosity of the air flow.

$$Re = \frac{|u_w - u_g| \cdot D_w}{\nu_g} \quad (7)$$

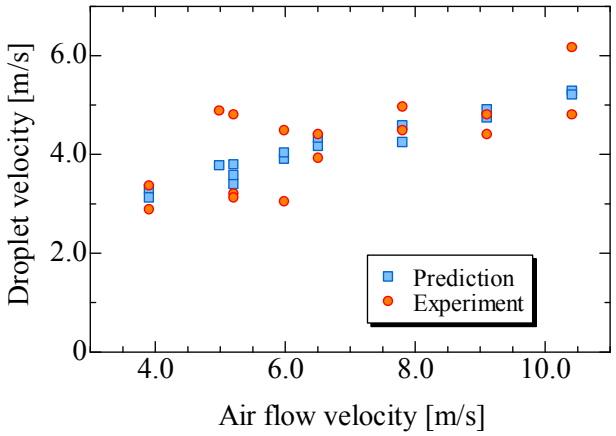


**FIGURE 7.** CORRELATION BETWEEN THE AIR FLOW VELOCITY AND THE DROPLET VELOCITY

Figure 8 shows the dimensionless displacements of the test rods in the droplet two-phase flow and those in the single-phase air flow for a comparison purpose. These displacements were obtained from analyzing the images recorded by the high speed camera, which views the side surface of test rod, by means of the motion tracking method provided by an image analyzing software. In the droplet two-phase flow, the vibration displacements were larger at almost all the Vr, especially at lower than 15, than those in the single-phase air flow. The dominant cause of this is that droplets collide with the test rod. This is also due to the effect of water droplets on the surface of the test rod: the water droplets on the surface make the cross-section area of the test rod against the flow larger, and then the aerodynamic pressure working on the test rod becomes larger.

Figure 9 shows a comparison of the R.M.S. power ratios between the single-phase flow and the droplet two-phase flow. At the Vr lower than 10, the R.M.S. power ratio regarding the single-phase flow has a peak because the dimensionless vibration displacements of the test-rod end in the Lift direction have a peak whereas those in the Drag direction have no peak. The test rod vibrations induced by the droplet two-phase flow have smaller bias of the kinetic energy of vibrations toward the Lift direction, compared to those induced by the single-phase flow. When the water droplets having the various sizes attach to the surface of the test rod, there are many different

characteristic scales surrounding the test rod, such as the height of an attached droplet, the diameter of the test rod and the sum of them. This may cancel large oscillation displacements in the Lift direction due to the vortex shedding.

Figure 10 shows the frequency spectra of the rod vibrations in the Lift and Drag directions for rod #1 in the case of $U_g$=6.0 m/s and these data on the graphs were obtained by the motion tracking method. In the single-phase air flow, there are prominent peaks at the natural frequency of each test rod. In contrast, no prominent peak is seen in the droplet two-phase flow. This is also because of the existence of several characteristic scales as discussed above.

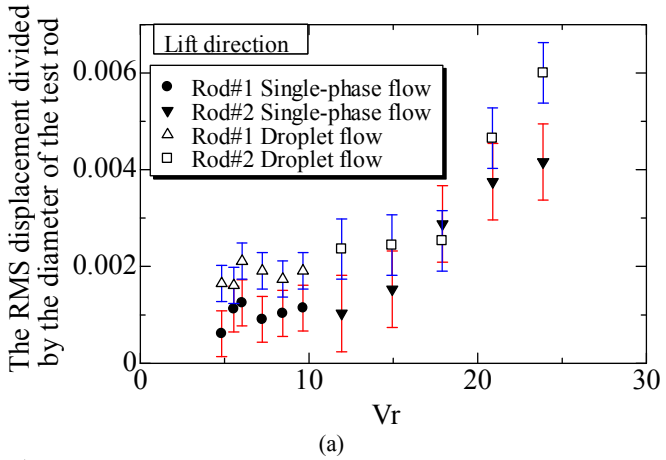


(a)

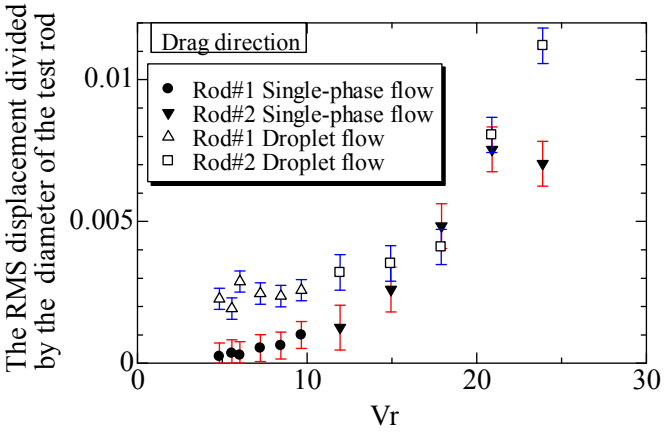


(b)

**FIGURE 8.** COMPARISON OF DIMENSIONLESS R.M.S. DISPLACEMENTS BETWEEN DROPLET TWO-PHASE FLOW AND SINGLE-PHASE FLOW
(a) Lift direction (b) Drag direction

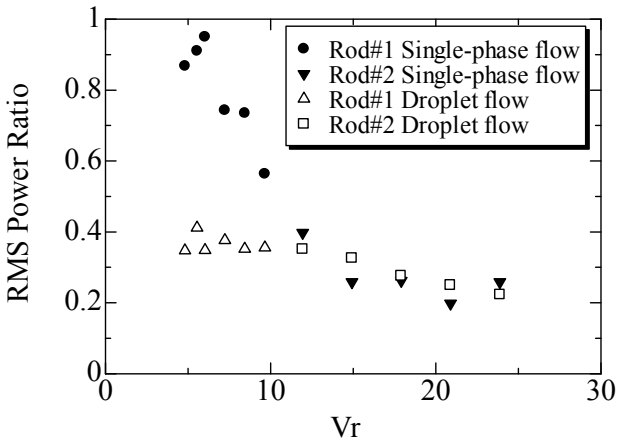


**FIGURE 9.** COMPARISON OF R.M.S. POWER RATIO $\sigma_{ratio}$ BETWEEN DROPLET TWO-PHASE FLOW AND SINGLE-PHASE FLOW

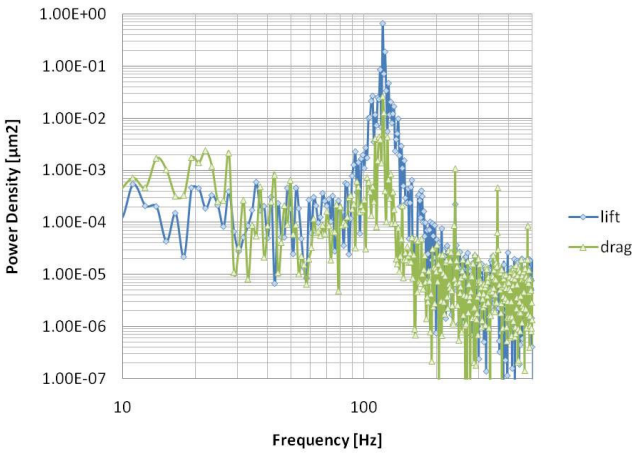


(a)

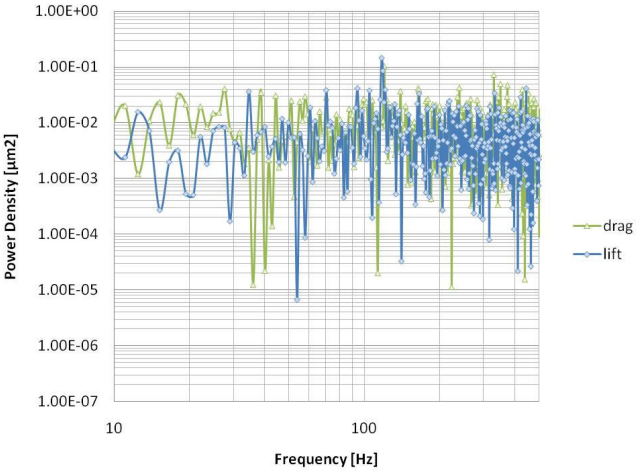


(b)

**FIGURE 10.** FREQUENCY SPECTRA OF ROD VIBRATIONS
(a) Single-phase air flow (b) Droplet two-phase flow

### 4.3 Comparison between Strain Gage Measurements and Motion Tracking Analyses

In both the single-phase flow and the droplet two-phase flow experiments, the test rod vibration amplitudes in both the Lift and the Drag directions was measured by two ways: the strain gage measurement and the motion tracking analysis. Figure 11 shows the dimensionless displacements in the single-phase flow measured by the strain gages and the motion tracking. The displacements in the Lift direction measured by the motion tracking have two peaks at the Vr of 6.0 and 9.1 whereas those measured by the strain gages have a peak at the Vr of 5.6. The motion tracking analyses evaluate the R.M.S. values of the dimensionless displacements larger than the strain gage measurements at every reduced velocity in regard to the Lift direction.

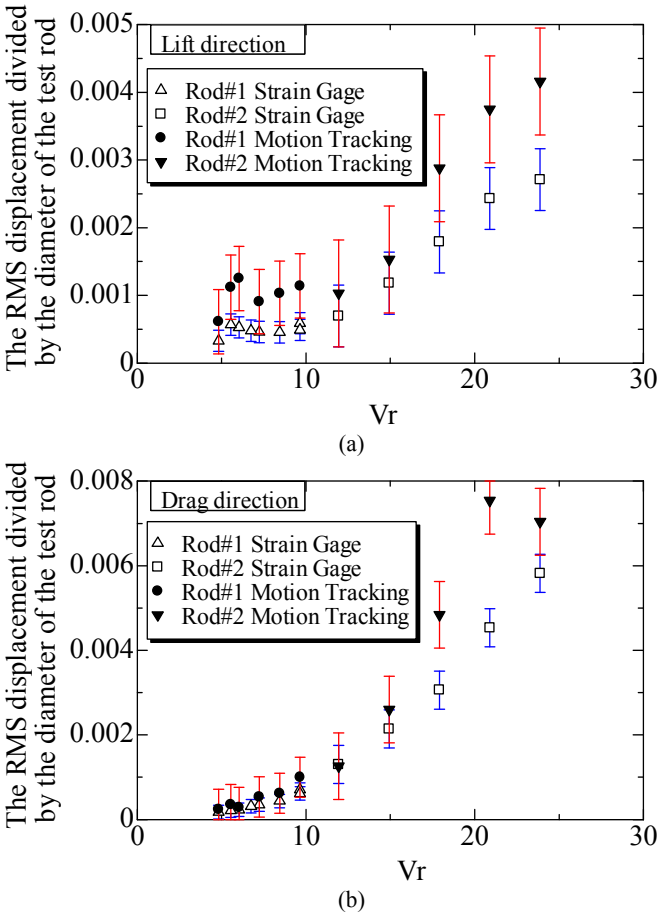


**FIGURE 11.** DIMENSIONLESS R.M.S. DISPLACEMENTS IN SINGLE-PHASE AIR FLOW
(a) Lift Direction (b) Drag Direction

On the other hand, the R.M.S. values of the dimensionless displacements in the Drag direction measured by the strain gages and the motion tracking correspond well with each other at the Vr lower than 15. At the higher Vr, the motion tracking analyses evaluate the displacements larger than the strain gages. This is because the high speed camera views directly the target mark carved on the side surface of the test rod whereas the strain gages detect the displacement of the test-rod end via the magnitude of strain at the position of themselves. The R.M.S. power ratios of the vibration displacements in the single-phase flow measured by the strain gages and the motion tracking are shown in Fig. 12, and they denote a similar tendency.

The dimensionless displacements in the droplet two-phase flow measured by the strain gages and the motion tracking are compared in Fig. 13. The dimensionless displacements both in the Lift and Drag directions show a good correspondence at the Vr higher than 15. However, at the Vr lower than 15, the motion tracking analyses evaluate the R.M.S. of the dimensionless displacements much larger than the strain gage measurements. This is because the flow was not uniform due to the droplets injection, and Eq. (2) that converts the measured strain into the displacement of the test-rod end can no longer be applied. In addition, the effect of the droplets collisions is considered to be another cause of these differences in the test rod displacements.

Figure 14 shows the comparison of the R.M.S. power ratio in regard to the dimensionless displacements in the droplet two-phase flow measured by the strain gages and the motion tracking. The power ratio measured by the strain gages seems to have a downward peak at around the Vr of 7.7-8.4, which indicates a strong bias of the kinetic energy of rod vibration toward the Drag direction. As the velocity of the flow decreases, the aerodynamic pressure becomes smaller, and then the droplets collisions to the test rod have more effects on the vibration amplitudes especially in the Drag direction.

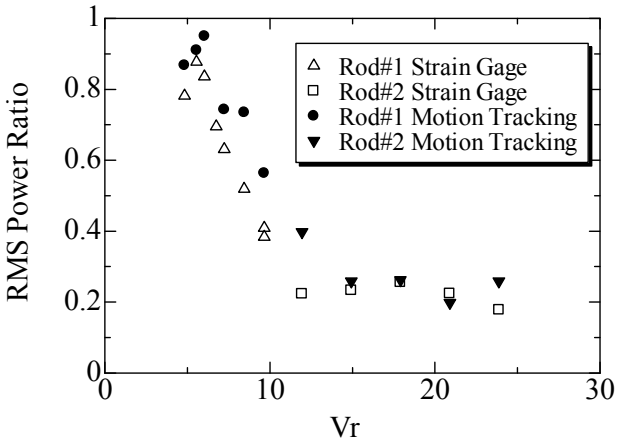


**FIGURE 12.** R.M.S. POWER RATIO $\sigma_{ratio}$ IN SINGLE-PHASE AIR FLOW

### 4.4 Effect of Droplets on Rod Surface

In the droplet two-phase flows, droplets on the test rods' surface are considered to change the turbulent structure around and downstream of the rod. In order to investigate the effect of

droplets on the surface qualitatively, numerical simulations were carried out by using the STREAM code (Software Cradle Co., Ltd.), a commercial code for 3D thermal-hydraulic analyses. The configuration of calculations is similar to that of the experiment in the present work, and in these calculations, the cylindrical rods are treated as fixed structures.

Three models of the test rod used in this simulation work are shown in Fig. 15. Model 1 is a cylinder with the diameter of 10 mm. Models 2 and 3 are combined structures of a cylinder with the diameter of 10 mm and four concentric cylinders with the thicker diameter and the axial length of 2 mm. These thicker cylinders represent the surface roughness due to droplets on the surface. The distance between the center points of any two adjacent thicker cylinders is 5 mm. The diameters of the thicker cylinder are 10.2 mm for Model 2 and 10.5 mm for Model 3, respectively. In these numerical simulations, 3D regular hexahedral mesh was used, and the mesh sizes are 0.5 mm for Model 1 and 0.25 mm for Model 2 and 3, respectively.

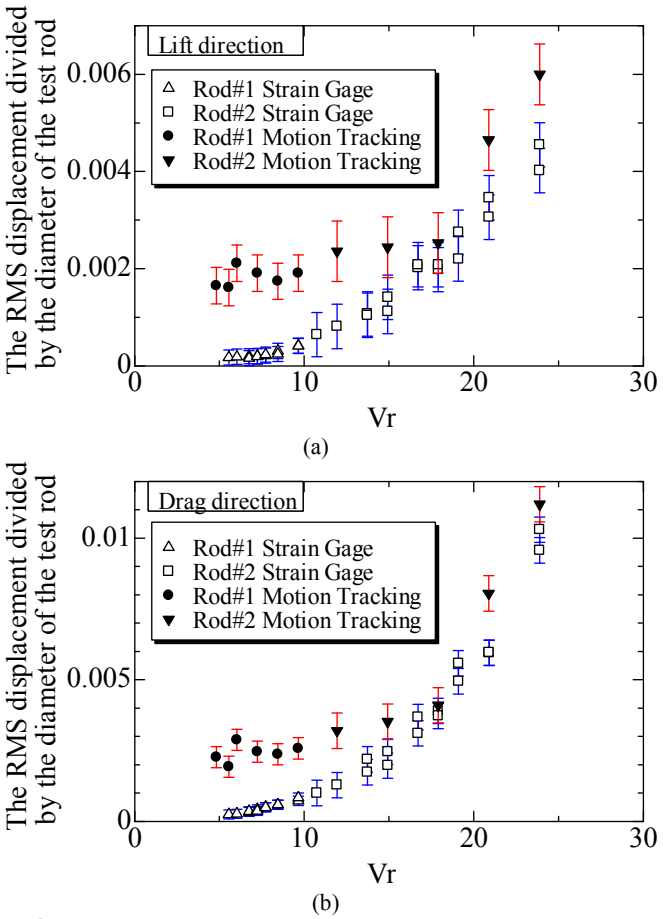


**FIGURE 13.** DIMENSIONLESS R.M.S. DISPLACEMENTS IN DROPLET TWO-PHASE FLOW
(a) Lift Direction (b) Drag Direction

The calculations were conducted using the standard k-ε turbulence model. Contour surfaces (red color) of turbulence energy at the same value for Model 2 and 3 are shown in Fig. 16. It is confirmed that the turbulence structures behind the cylindrical rod are affected by the surface projections, even though the roughness of the thicker cylinders is as low as 2 % in radius.

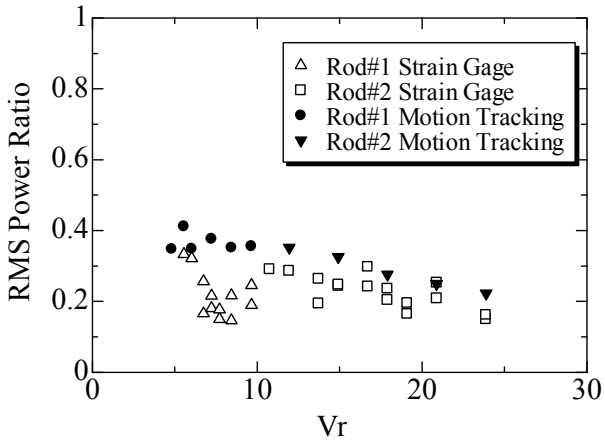


**FIGURE 14.** R.M.S. POWER RATIO $\sigma_{ratio}$ IN DROPLET TWO-PHASE FLOW

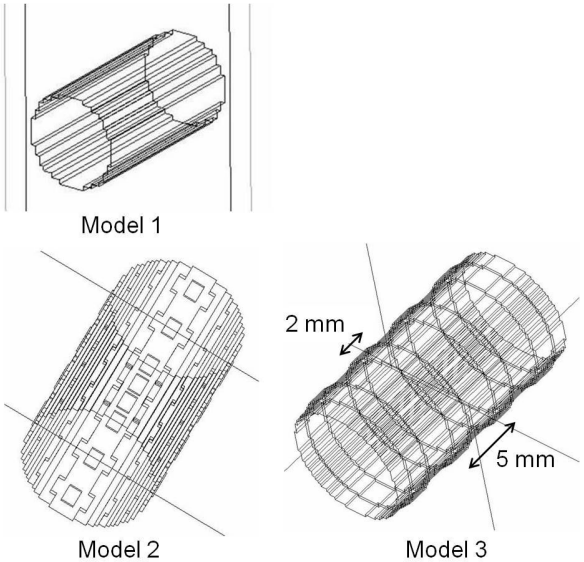


**FIGURE 15.** MODELS OF CYLINDERS

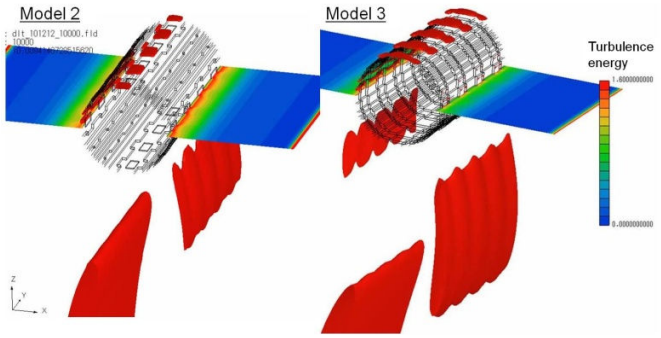


(a) (b)

**FIGURE 16.** CONTOUR OF TURBULENCE ENERGY
(a) Model 2 (b) Model 3

## 5. CONCLUSIONS

The R.M.S. displacements of the test rod vibration induced by the single-phase air flow have two peaks in the Lift direction at the reduced velocity Vr of 5.6 for the test rod #1 and 7.7 for the test rod #3. From the image analyses by means of the motion tracking method, the vibration displacements of the test rod in the droplet two-phase flow are found to be larger at almost all Vr, especially at the Vr lower than 15, than those in the single-phase air flow. This is because the water droplets attached to the curved surface of the test rod make the cross-section area of the test rod larger against the flow, and then the aerodynamic pressure working on the test rod becomes larger. On the other hand, the test rod vibrations induced by the droplet two-phase flow have smaller bias of the kinetic energy of vibration toward the Lift direction at the Vr around 6.0 where the vibration in the single-phase flow have a strong bias of the kinetic energy toward the Lift direction.

The dimensionless displacements measured by the strain gages and motion tracking analyses show some differences in the dimensionless displacements. Through all the experiments in the present study, it can be said that the strain gage measurements evaluate the test rod vibration smaller than the motion tracking analyses except larger Vr regions. This is because high speed camera views directly the target mark carved on the side surface of test rod whereas the strain gages detect the displacement of the rod end via the magnitude of strain at the position of themselves.

## REFERENCES

[1] Pettigrew, M.J. and Taylor, C.E., 2003. "Vibration analysis of shell-and-tube heat exchangers: an overview Part 1:flow, damping, fluidelastic instability," *Journal of Fluids and Structures*, 18, pp. 469-483.

[2] Hara, F., 1982. *Journal of the Japan Society of Mechanical Engineers Ser. C*, 48. 433, pp. 1371-1379.

[3] Hara, F. and Ogawa, N., 1983. "Vibrations of a Circular Cylinder Immersed Perpendicular to a Two-Phase Air-Water Bubbly Flow," *Journal of the Japan Society of Mechanical Engineers Ser. C*, 49. 455, pp. 1624-1629.

[4] Ogawa, N. and Hara, F., 1984. *Journal of the Japan Society of Mechanical Engineers Ser. C*, 50. 459, pp. 2086-2093.

[5] Nakamura, T. et al., 1986. "A Study on the Flow Induced Vibration of a Tube Array by a Two-Phase Flow," *Journal of the Japan Society of Mechanical Engineers Ser. C*, 52. 483, pp. 2790-2795.

[6] Funakawa, M. *et al.*, 1989. "Vibration of Tube Arrays Induced by Two Phase Normal Flow," *Journal of the Japan Society of Mechanical Engineers Ser. C*, 55. 519, pp. 2718-2723.

[7] Axisa, F. Antunes, J. and Villard, B., 1990. "Random Excitation of Heat Exchanger Tubes by Cross-Flows," *Journal of Fluids and Structures*, **4**, pp. 321-341.

[8] Matsumoto, M. *et al.*, 2002. "Investigations on Wind-induced Vibrations of Stay-cables Based on Field Observations and Wind Tunnel Tests," *Kyoto Univ. Disaster Prevention Research Institute Annuals*, 46, pp. 319-329.

[9] Yamaguchi, H., 1990. "Analytical Study on Growth Mechanism of Rain Vibration of Cables," *Journal of Wind and Industrial Aerodynamics,* 33, pp. 73-80.

[10] Hikami, Y. and Shiraishi, N., 1988. "Rain-Wind Induced Vibrations of Cables in Cable Stayed Bridges," *Journal of Wind Engineering and Industrial Aerodynamics*, 29, pp. 409-418.

[11] Matsumoto, M. *et al.*, 1989. "Experimental Studies on Rain-Wind Induced Vibration of Inclined Cables," *Kyoto Univ. Disaster Prevention Research Institute Annuals. B*, 32(B-1), pp. 471-482.

[12] Naudascher, E. and Rockwell, D., 1994. "Flow-Induced Vibrations: An Engineering Guid," Dover Publications, INC.

[13] Murata, H. *et al.*, 2003. *National Maritime Research Institute in Japan Conference Papers*, PNM2A030059.

[14] Fujita, K. and Ito, 2000. T., *Journal of the Japan Society of Mechanical Engineers Ser. C*, 66. 643, pp. 715-723.

[15] Naudascher, E., 1987. "Flow-Induced Streamwise Vibrations of Structures," *Journal of Fluids and Structures*, **1**, pp. 265-298.

[16] Haider, A. and Levenspiel, O., 1989. "Drag Coefficient and Terminal Velocity of Spherical and Nonspherical particles," *Powder Technology*, 58, pp. 63-70.